HOSTED BY
ELSEVIER
CrossMark
Available online at www.sciencedirect.com
ScienceDirect
Defence Technology 11 (2015) 1–9
www.elsevier.com/locate/dt

Strain rate dependency and fragmentation pattern of expanding warheads

John F. MOXNES [a,*], Anne K. PRYTZ [b,2], Øyvind FRØYLAND [a,1], Stian SKRIUDALEN [a,1], Steinar BØRVE [a,1], Gard ØDEGÅRDSTUEN [b,2]

[a] *Land Systems Division, Norwegian Defence Research Establishment (FFI), P.O. Box 25, NO-2027 Kjeller, Norway*
[b] *Nammo Raufoss AS, P.O. Box 162, NO-2831 Raufoss, Norway*

Received 3 July 2014; revised 26 August 2014; accepted 27 August 2014
Available online 22 December 2014

Abstract

For the characterization of the behaviors of a metal material in events like expanding warheads, it is necessary to know its strength and ductility at high strain rates, around 10^4–10^5/s. The flyer plate impact testing produces the uniform stress and strain rates but the testing is expensive. The Taylor test is relatively inexpensive but produces non-uniform stress and strain fields, and the results are not so easily inferred for material modeling. In the split-Hopkinson bar (SHB), which may be used in compression, tension and torsion testing, the strain rates never exceeds 10^3/s. In the present work, we use the expanding ring test where the strain rate is 10^4–10^5/s. A streak camera is used to examine the expanding ring velocity, and a water tank is used to collect the fragments. The experimental results are compared with the numerical simulations using the hydrocodes AUTODYN, IMPETUS Afea and a regularized smooth particle (RSPH) software. The number of fragments increases with the increase in the expansion velocity of the rings. The number of fragments is similar to the experimental results. The RSPH software shows much the same results as the AUTODYN where the Lagrangian solver is used for the ring. The IMPETUS Afea solver shows a somewhat different fragmentation characteristic due to the node splitting algorithm that induces pronounced tensile splitting.

Keywords: Warhead; Fragmentation; Simulation; Fracture model; Expanding ring

1. Introduction

Plasticity-based analytical modeling and finite element methods (FEM) may be used to predict the fragmentation pattern of warheads. However, the viability of the predictions relies on the material constitutive models describing the plastic flow stress and fracture. For an expanding thin wall casing, the tangential strain rates are typically in the range of 10^4–10^5/s and the quasi static established material model may not be viable. Main research issues are the dependency of fracture strain on triaxiality (that means on the proportion of invariant I_1 to J_2), the influence of the third invariant, i.e., strain rate, on ductility, element size and the connection to adiabatic shear bands at high strain rate, and whether statistical failure predicts the size distribution of fragments better than a homogeneous failure model [1–6].

Failure process of ductile materials is caused by the nucleation, growth and coalescence of voids to fracture. The fracture coalescence depends on pressure or triaxiality (that means on the proportion of invariant I_1 to J_2) [7]. In general, the larger the triaxiality is, the smaller the fracture strain at failure becomes. This is in agreement with theoretical models for void growth [8,9]. Recently, Bao and Wierzbicki [10,11] compared the different models to cover the influence of triaxiality. They concluded that none of the models were able to capture the fracture behavior in the entire range of triaxiality. The void growth was the dominated ductile failure mode

* Corresponding author. Tel.: +47 63 807514, +47 63 807000; fax: +47 63 807509.
E-mail address: john-f.moxnes@ffi.no (J.F. MOXNES).
Peer review under responsibility of China Ordnance Society.
[1] Tel.: +47 63 807000.
[2] Tel.:+47 61 153609.

http://dx.doi.org/10.1016/j.dt.2014.08.006

at large triaxialities (say above 0.4), while the shear of voids dominates at low triaxialities. The main conclusion was that there was indeed a possible slope discontinuity in the fracture locus corresponding to the point of fracture transition [11]. A dependency of the third invariant has been forecasted.

Both yield strength and ultimate tensile strength usually increase with strain rate for steel materials. The ductility of quenched and tempered steel may increase with strain rate, while the ductility of the material which high strength is achieved by precipitation hardening process may decrease with strain rate. Body-centered cubic (bcc) materials can also behave different from face-centered cubic (fcc) materials. Thermal softening decreases strength and increases ductility. Thus the ductility of materials could increase with small strain rates but could decrease with higher strain rates due to thermal softening. Decreased ductility at higher strain rates may be explained by shear localization due to adiabatic heating [12]. Unstable adiabatic shear transfers the entire burden of strain to a finite number of these shear planes (adiabatic shear bands). Due to restriction on computational time, the element sizes are traditionally too coarse to resolve the shear bands by direct simulation.

Wilkins et al. [13] concluded many years ago that the order of the applied loads, i.e. hydrostatic pressure followed by shear or vice versa, should be important in failure modeling. To account for the order of the applied loads, the cumulative damage criterion has been applied [13]. Fracture occurs at a point of the material where a weighted measure of the accumulated plastic strain reaches a critical value. The weighing function depends on the triaxiality and/or the third invariant I_3. Finding an appropriate weighting function is still an active field of research [14,15]. In the Johnson–Cook (J–C) model [16], an uncoupled (passive) damage evolution formulation with no third invariant dependency is adopted, which entails that there is no coupling between the stress-strain behavior and the damage evolution until fracture occurs at the critical damage.

The split-Hopkinson bar (SHB), which may be used in compression, tension and torsion testing, is the most widespread method for material high strain rate characterization. However the strain rate never exceeds 10^3/s and is thus much lower than that achieved under explosive loadings. Many ductile materials display an increase in yield stress for strain rates above 10^3/s [17,18]. It is challenging to conduct material tests at the strain rates of larger than 10^3/s. The flyer plate impact testing produce uniform stress and strain rates but the testing is expensive. The Taylor testing is relatively inexpensive and data could be obtained from simple post-test measurements. However, the Taylor test produces non-uniform stress and strain fields and the results are not so easily interpreted for material modeling.

In this article, the fracture behavior of steel rings, taken from a 25 mm warhead, is studied. To reach the strain rates of more than 10^3/s, an expanding ring test is performed. A streak camera was used to examine the ring velocity, and a water tank was used to collect the fragments [19].

A quasi static strength model of the steel was established by using a smooth uniaxial tensile test to find the von Mises flow plastic function in a J–C strength model. The parameters of a J–C damage development model are found using the results from quasi static tensile tests in which three different sample geometries are used [20].

The Lagrangian processor is computationally fast and gives good definition of material interfaces. However, the ability of the Lagrangian processor to simulate explosive events can only be enhanced by use of an erosion algorithm which removes the zones that have reached a user-specific strain, typically in the order of 75%–150%. The Eulerian processor, which uses a fixed grid through which material flows, is much more expensive in calculation than the Lagrangian processor, but is well suited for modeling larger deformations and fluid flow. See Refs. [21,22] for use of Eulerian CTH code. See Refs. [23,24] for use of the Arbitrary-Lagrangian-Eulerian ALE3D/CALE codes and Ref. [25] for semi-empirical-numerical methods.

The smooth particle hydrodynamics (SPH) method is a Lagrangian technique [26]. This grid-less technique does not suffer from the problem associated with the Lagrangian technique of grid tangling in large deformation problems. SPH is based on two main approximations of the continuum equations. First, an arbitrary scalar field variable is described by an integral over the space that is only approximate since a smoothed kernel is used in the integral instead of the exact Dirac delta function. Second, this integral is approximated by a discrete sum of a finite set of interpolation points (the particles). In AUTODYN and LS-DYNA, SPH nodes interact with Lagrangian surfaces. This allows to model the regions which undergo small deformations using the Lagrangian processor, while those regions experiencing large deformations (i.e. the explosive) can be modeled using SPH. The most well-known problem with SPH is loss of stability due to tensile instability and artificial fragmentation due to large particle spacing relative to the smoothing length. Regularized smooth particle hydrodynamics (RSPH) was developed to increase accuracy in shock wave modeling [27]. In the current work, the original RSPH code has been extended to study the fragmentation of solids with a state of the art handling of tensile instability [28] and a sufficiently small ratio between the original particle spacing and the smoothing length.

We also apply the IMPETUS Afea node splitting algorithm and the corpuscular model. The corpuscular method does not start from the continuum equations, but postulate a number of particles that interact by collisions [29,30]. In the Lagrangian solver, instead of eroding cells that fails, the nodes can split, resulting in a sort of crack propagation. These cracks are constrained by the mesh, or cell size.

2. Experimental setup and geometrical data

Figs. 1 and 2 show the setup. The brass tubes with constant outside diameter and variable inside diameter were loaded with the explosive, which is modeled as composition LX10. Steel rings were manufactured from projectile bodies of the in-service round. To find the velocity of the rings, the test item is placed such that the expansion of the ring is perpendicular to

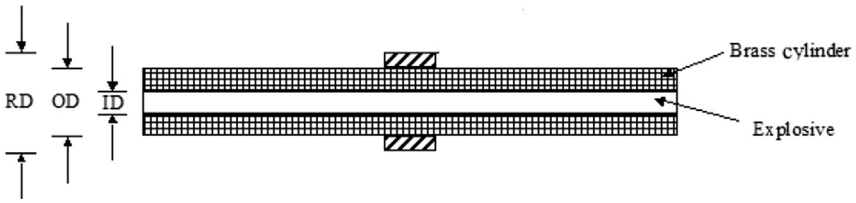

Fig. 1. The material locations and the geometrical setup for the expanding ring test.

the axis of a rotating mirror camera. The fragmentation studies were a duplication of the streak camera studies. However, in this case the fragments were collected in a water tank. To be able to repeat the actual velocity-time conditions, the tubes and rings were allowed to expand first in a thin plastic bag filled with air that was submerged underwater. Thus the expansions and break-up occurred in air. The water barrel was then emptied and sieved, and the fragments were collected with a magnet. More than 95% of ring mass was collected.

The explosive was ignited at one end of the cylinder at time zero. The density of the explosive was 1.87 g/cm^3, and the detonation velocity was 8820 m/s. The AUTODYN "burn on time" model was used for the explosive. The total length of the cylinder with explosive is 10.2 cm. The length of the steel ring is 1 cm and its thickness is 0.3 cm. Two different shots (loadings) were studied (Table 1).

3. Strength and fracture/failure model of steel ring

The uniaxial tensile test specimens and two notched tensile specimens were extracted from a heat-treated steel material to establish a J–C strength and failure/fracture model. The steel alloy composition is provided in Table 2. The steel is first casted, then rolled and heat-treated by quenching. Finally it is tempered. The hardness is 530 Vickers (5.6 GPa).

The tests were carried out at room temperature in a hydraulic test machine with a strain rate of approximately 5×10^{-4} s^{-1} (quasi static condition). The numerical simulations of the mechanical tests were performed, assuming the properties of isotropic material. The results were compared with the experimental results [20].

The J–C [16] strength model is

$$\sigma = Y(\varepsilon_p)\left(1 + c\ln\left(\dot{\varepsilon}_p \Big/ \dot{\varepsilon}_p^*\right)\right)\left(1 - \left(\frac{T - T_{room}}{T_{melt} - T_{room}}\right)^m\right) \quad (1)$$

where $Y(\varepsilon_p)$ is set as a piecewise linear function of the plastic strain, ε_p, vs. stress, Y, in MPa to read: {{0, 1352.5}, {0.005, 1518.68}, {0.015, 1680.13}, {0.025, 1742.46}, {0.035, 1775.2}, {0.045, 1796.74}, {0.0460, 1798.56}, {0.146001, 1864.57}, {0.346001, 1958.05}, {0.657603, 2089.82}, {2, 2580.7}}; c is the strain rate parameter that is set to zero for the quasi static tests and as the baseline value;$\dot{\varepsilon}_p$ is the plastic strain rate;$\dot{\varepsilon}_p^*$ is the nominal plastic strain rate of 1/s. T_{room} is the reference temperature set to 300 K; and T_{melt} is the melting temperature set to 1800 K. For the quasi static tensile tests, we set that $T = T_{room}$. Other properties given for this steel is $E = 210$ GPa as the elastic modulus, $\nu = 0.33$ as the Poisson ratio and $\rho = 7850$ kg/m^3 as the density.

The J–C [16] damage development model is

$$\frac{\partial D}{\partial \varepsilon_p} = \frac{1}{\varepsilon^f(\sigma^*)},\ \varepsilon^f(\sigma^*) = \left(D_1 + D_2 \mathrm{Exp}\left(-D_3\sigma^*\right)\right) \times \left(1 + D_4 \ln\left(\dot{\varepsilon}_p \Big/ \dot{\varepsilon}_p^*\right)\right) \quad (2)$$

where σ^* is the triaxiality (negative value of pressure/Mises stress ratio). The experimental results for this steel give $D_1 = 0.069$, $D_2 = 10.8$ and $D_3 = 4.8$ [20]. We set the strain rate parameter, $D_4 = 0$, as baseline value.

The brass was simulated by using the Johnson–Cook strength function with yield strength of 112 MPa, the hardening constant of 505 MPa, and the hardening exponent $n = 0.42$.

4. Results

Fig. 3 shows a picture of the 3D simulation of the experimental setup in AUTODYN. The simulations were performed in 3D using quarter symmetry. In AUTODYN and IMPETUS the unstructured grid with 4-noded tetrahedral elements are used. The SPH algorithm was used for the explosive, brass and ring. The very same simulation was performed in IMPETUS

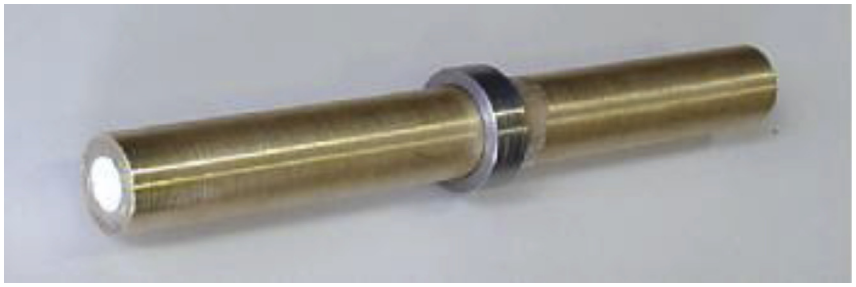

Fig. 2. The expanding ring test.

Table 1
Dimensions of brass cylinder.

	OD/cm	ID/cm
Loading 1	1.83	0.52
Loading 2	1.83	1.25

Table 2
Steel alloy composition in percent.

Fe	C	Mn	Cr
Balance	0.28	1.25	0.5

Afea; however, here the corpuscular model was used for the explosive and the Lagrange model for the steel ring and the brass. The node splitting algorithm was used for the steel ring only.

Fig. 4 compares the streak camera recordings with the simulations for two different shots.

IMPETUS Afea and AUTODYN show more or less the same results. The experimental results are scattered but in good agreement with the simulations. The sharp increase in the measured velocity for the high velocity shot, at around 25 μs, is likely due to gas leakage that was recorded by the streak camera.

The initial velocity of the ring is due to the grazing detonation wave. As the explosive products continue to drive the ring, the fractures begin to form and the acceleration of ring takes place. As the cracks coalesce and the fragments are formed, the explosive products begin to leak between the fragments and the acceleration decreases. The fragments have thus reached their final velocity.

The fragmentation pattern may depend on the numerical solver. Only the rings were used in a numerical study. The expansion velocities of the rings in Fig. 4 were input to new simulations where we apply different numerical techniques. 190 m/s expansion velocity was used for the low velocity and 630 m/s for the high velocity shot. For the low velocity we apply an element size of 600 microns in 3D as baseline. For the high velocity we apply quarter of symmetry in 3D and an element size of 400 microns. The experimental results are compared with the numerical simulations using the AUTODYN, IMPETUS Afea and the regularized smooth particle (RSPH) method. In AUTODYN, we used element erosion at the strain of 1.5. In the IMPETUS Afea, erosion by material failure was used for the brass tube. The mass of the steel ring is preserved due to the node splitting algorithm. However, for

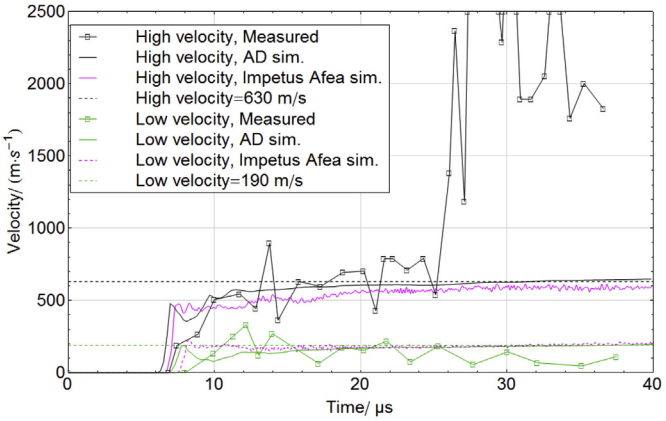

Fig. 4. The simulated and experimental velocities of the expanding rings.

the high velocity case (only), erosion due to falling time step had to be utilized in order to avoid the numerical problems, only about 1.4% was eroded in this case. No erosion was used for the steel ring in the low velocity case and hence the fracturing of the ring is solely due to the node splitting algorithm.

Figs.5–8 show the simulation results for baseline parametric values with $T = T_{\text{room}}$. We apply symmetry and only simulate half of the ring along the axial axes. Fig. 5 shows the results after 6 μs for the high velocity shot. In AUTODYN, a layer connected to the inner surface of the ring is severely damaged and failed. Failure develops from this region and spreads outwards by tensile, or shear, failure. In IMPETUS Afea, the node splitting algorithm controls the fracture. The node splitted region spreads outwards and radially. The RSPH shows much the same behavior as in AUTODYN although the severe damaged region at the inner surface is not observed.

Fig. 6 shows the results after 20 μs. The symmetry plane is clearly seen. The number of the larger fragments is around 30–300.

Figs.7 and 8 show the similar results for the low velocity shot in IMPETUS Afea and RSPH. AUTODYN did not show any fractures. In general, the number of fragments is much lower than that for the high velocity shot. The reduced number of fragments can be explained. The fragmentation process starts with the initiation of shear or tensile fractures at some random points. After fractures are initiated, loads decrease so stresses are not sufficient to trigger the multiple fracture surfaces. However, when the same ring is deformed at high strain rate, the fragmentation number increases since a fracture that develops at one location can only influence the stress and

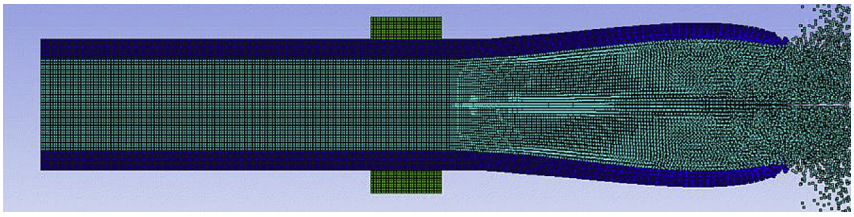

Fig. 3. A picture of the simulation in AUTODYN.

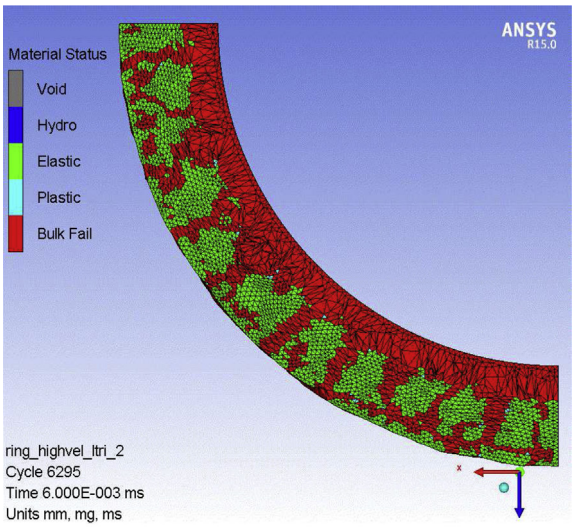

(a) AUTODYN

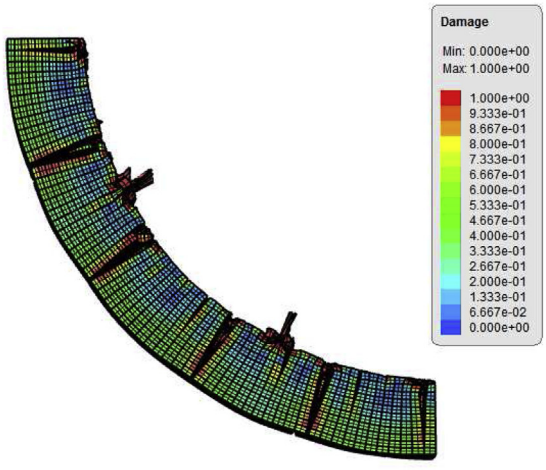

(b) IMPETUS Afea

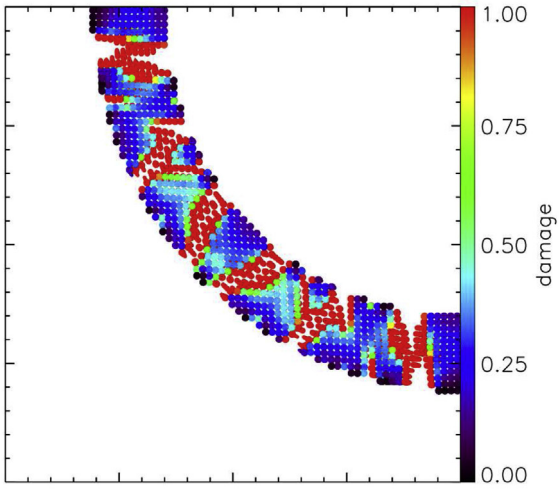

(c) RSPH

Fig. 5. The fragmentation/failure patterns at 6 μs with the ring expansion velocity of 630 m/s.

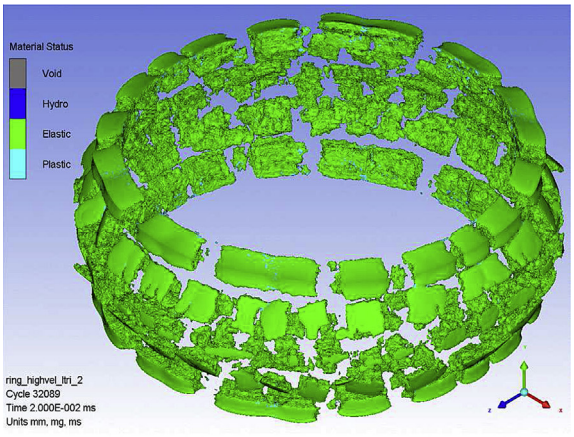

(a) AUTODYN

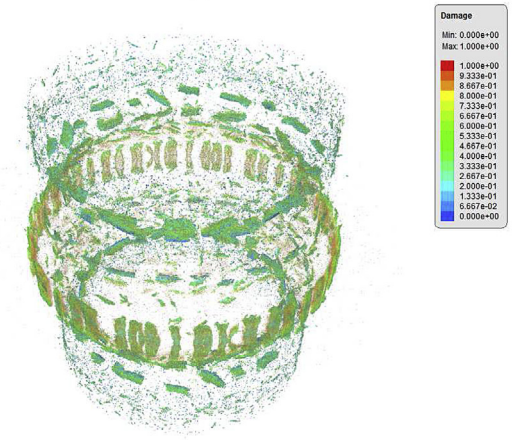

(b) IMPETUS Afea

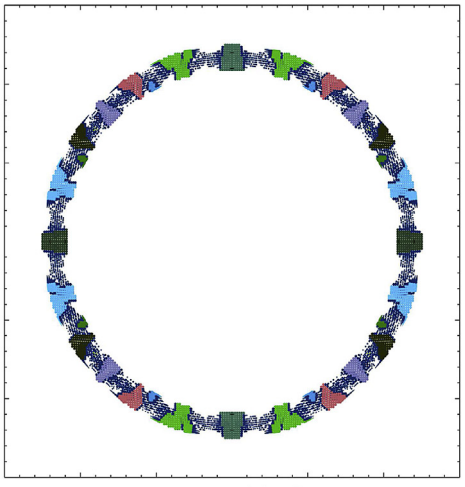

(c) RSPH

Fig. 6. The fragmentation/failure patterns at 20 μs with the ring expansion velocity of 630 m/s.

strain at a neighboring location after a finite delay time. This delayed interaction between initiation sites provides time for crack growth at neighboring sites.

In AUTODYN and RSPH, the temperature of the element cells was never increased to more than 100 K, and applying temperature softening did not significantly influence the

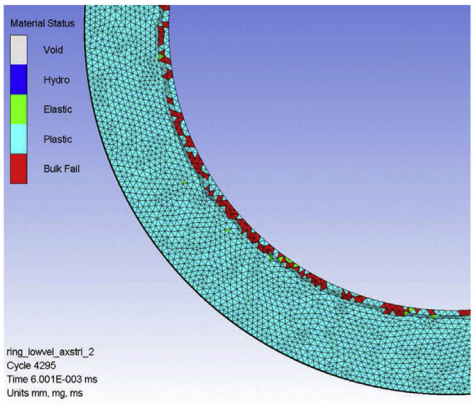

(a) AUTODYN-3D

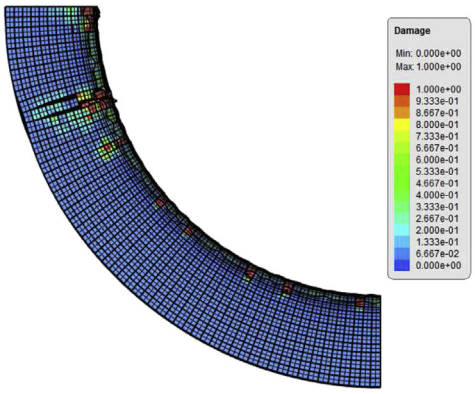

(b) IMPETUS Afea

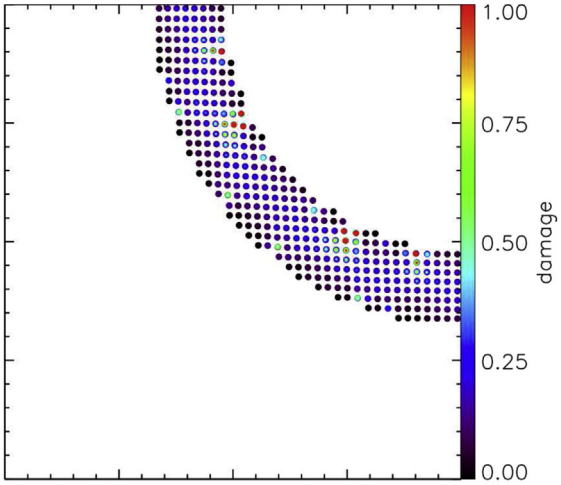

(c) RSPH

Fig. 7. The fragmentation/failure patterns at 6 μs with the ring expansion velocity of 190 m/s.

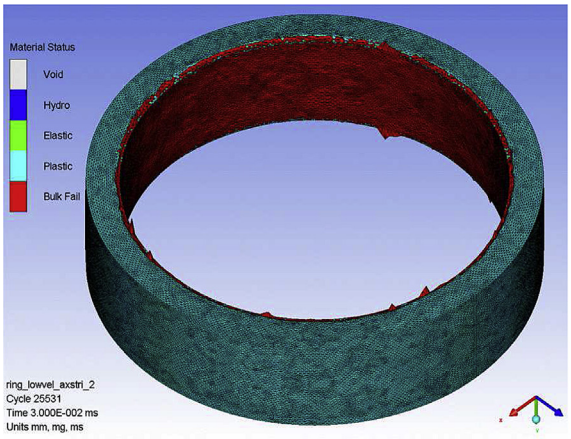

(a) AUTODYN

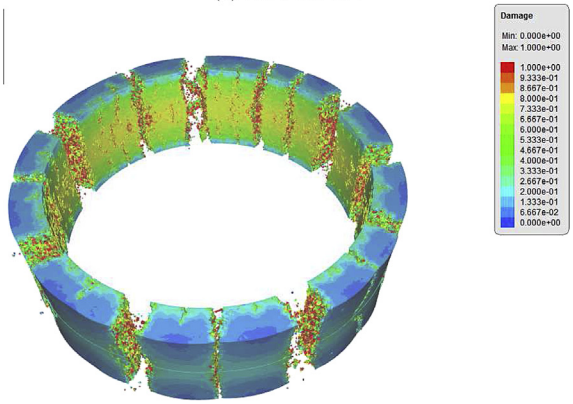

(b) IMPETUS Afea

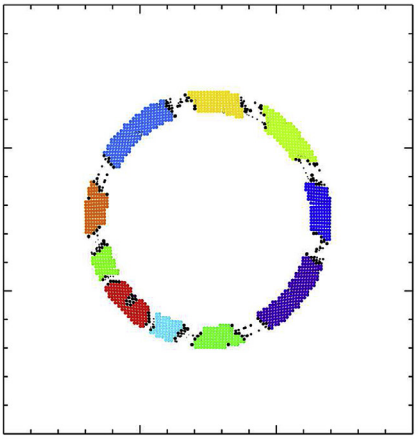

(c) RSPH

Fig. 8. The fragmentation patterns at 30 μs with the ring expansion velocity of 190 m/s.

fragmentation pattern (data not shown). In the AUTODYN and IMPETUS Afea simulations, the energy error was lower than one percent at the time of crack generation. The error was not increasing with time.

For strain rates up to 10^3/s, it is believed that the dislocation motion is controlled by thermal activation, and a linear logarithmic relationship has traditionally been used for strength as a function of strain rate [16]. Above the rate of 10^3/s, the strength of materials are often significantly enhanced [16,18,31] due to the changes of the microstructure rate controlling mechanisms. Enhanced strain rate dependency may be due to resistance to dislocation motion in the lattice itself by phonon viscosity [32]. The stress is here found to be linearly proportional to the strain rate [33]. In Ref. [20], the ring

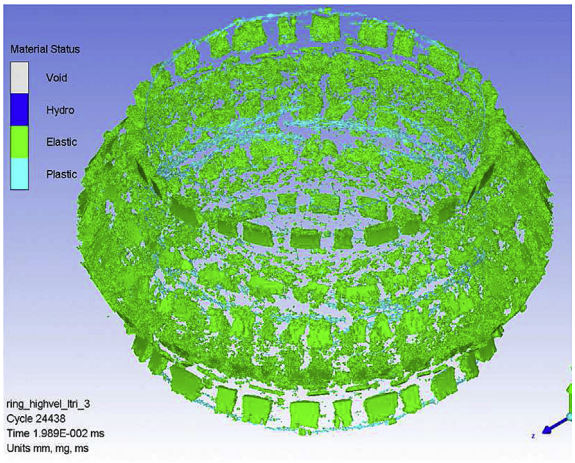

(a) AUTODYN-3D

(b) D4 = −0.08, RSPH-2D

Fig. 9. The fragmentation/failure patterns at 20 μs with the ring expansion velocity of 630 m/s.

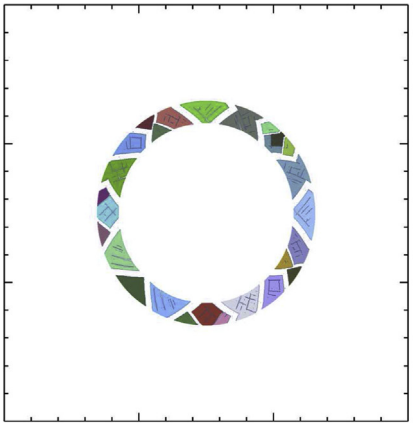

(a) RSPH-2D

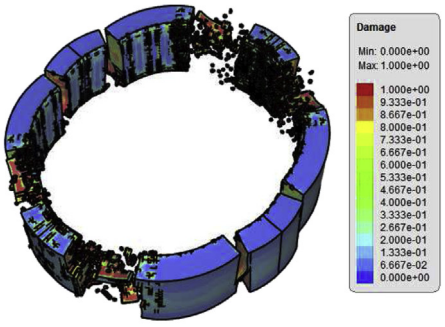

(b) IMPETUS Afea (with explosive)

(c) Experiment 190 m/s

Fig. 10. The fragmentation pattern at 30 μs with the ring expansion velocity of 190 m/s.

material was studied, and it was found that the simulation results worsen when the strength increases with strain rate.

Shear localization due to adiabatic shear band that is much smaller than the element size can soften the material and increase the ductility material. This unstable thermoplastic shear occurs locally in the shear bands when the local flow stress decreases with the increase in strain. This happens when the rate of thermal softening due to the internally generated heat exceeds the rate of isothermal work hardening. The greater the shear strain rate is, the larger the number of these shear bands becomes, and hence there is a lower stress for a given strain on the element level.

The thickness of adiabatic shear bands may be not more than 10 microns. Thus our 3D grid was likely too coarse to resolve shear bands by the direct simulation. However, in an attempt to improve the simulation, we applied RSPH-2D simulations (infinite long cylinder) with a grid size (particle size) of around 40 microns. For the high velocity, we applied a quarter symmetry.

Comparing the 3D results in Figs.5 and 8 with the RSPH-2D results in Figs.9 and 10, it appears that the shear failure is more significant in 2D. The reason whether this is due to the grid size per se or due to the 2D assumption per se is not explained.

Fig. 9 shows, compared with Fig. 6, that the number of fragments increases when the ductility decreases with strain rate ($D_4 = -0.08$). Figs. 10 and 8 show for IMPETUS Afea that the simulation with the explosive is similar to the simulation with the radial expansion velocity only.

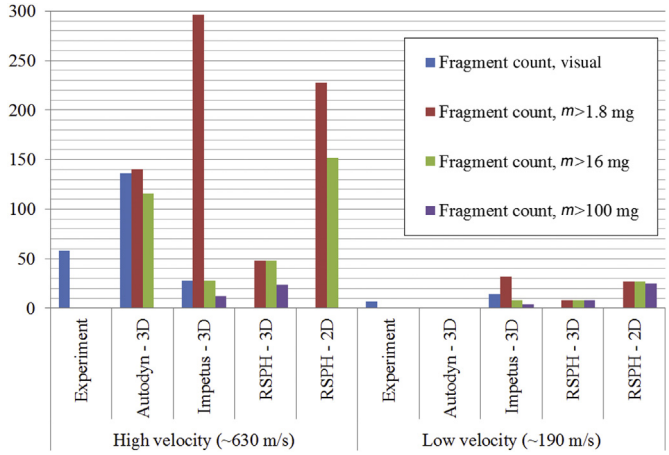

Fig. 11. The number of fragments from experiment and software simulations.

Meyer and Brannon [1] used a Weibull distributing to generate statistical failure that predicts the size distribution of fragments better than a homogeneous failure model. Applying this approach to the ring may enhance the fragmentation of steel [2–6]. The AUTODYN low velocity results above may indicate that the statistical failure is necessary for some solvers if the elements are too small.

Fig. 11 shows the simulated and experimental number of fragments. The experimental and simulated results are similar. However, in general the number of fragments is too large. The exception is the low velocity AUTODYN simulation that shows only one fragment. Fig. 12 shows the variability of the fragment count when applying different smoothing lengths h and statistical failure in the RSPH. The D_2 parameter in the J–C model is stochastic according to a Weibull distribution (see Ref. [1]).

5. Conclusions and discussion

The fracture behavior of the steel rings made of a casing of 25 mm warhead was studied experimentally and numerically. The parameters of a J–C strength and fracture model were established using the results from tensile tests of the smoothed bar and two notched bars. The simulated expansion velocity of the rings matches the streak camera measurements.

Two different expansion velocities of the steel ring were studied. The number of fragments increases with the increase in expansion velocity of the rings. The number of fragments was similar to the experimental results. The RSPH shows the same results as those the AUTODYN gives for the high velocity shot. The IMPETUS Afea shows a somewhat different fragmentation characteristic due to the node splitting algorithm that induces pronounced tensile splitting.

Applying 2D in RSPH simulation with a grid size of around 40 microns, i.e. one order of magnitude lower than in 3D, showed a higher number of shear fractures at the inner surface of the ring. The effect was more visible at the lower velocity. The low velocity shot in AUTODYN did not show any fractures for chosen grid. This may highlight the necessity of applying statistical failure instead of homogeneous failure. A numerical computed chaotic trajectory diverges exponentially from the true trajectory with the same initial condition. However, there exists an errorless trajectory (no computational error) with slightly different initial condition, which stays near (shadows) the numerical computed one. Thus a computational solution with no variation in the initial conditions may mimic the true solution with the variations in the initial conditions [34].

The number of fragments in AUTODYN increased when the ductility decreased with strain rate.

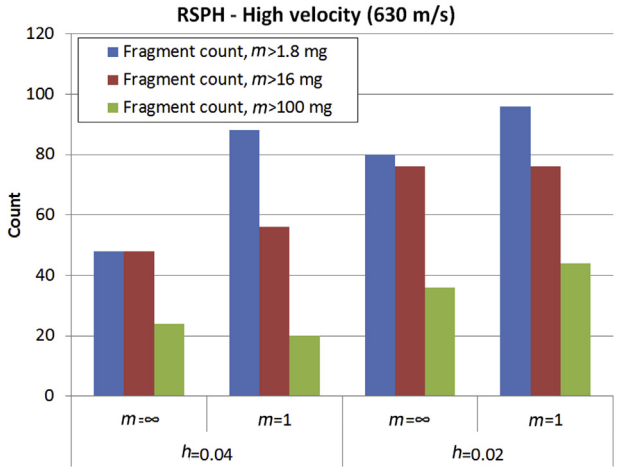

Fig. 12. Variability of fragment count with smoothing length (h) and statistical failure (M).

References

[1] Meyer HW, Brannon RM. A model for statistical variation of fracture properties in a continuum mechanics code. Int J Impact Eng 2012;42:48–58.
[2] Haldorsen Tom, Moxnes John F. Fragmentation of a steel ring by use of C-4. FFI/Report-98/03004. Forsvarets Forskningsinstitutt; 1998 (Approved for public release).
[3] Haldorsen Tom, Moxnes John F. A fragmentation model for the multi-purpose round. FFI/Report-98/04940. 1998.
[4] Diep QB, Moxnes JF, Ødergårdstuen G. A fragmentation model in 3D based on stochastic noise. In: Autodyn User Group Meeting, England; 2000.
[5] Diep QB, Moxnes JF, Nevstad G. Fragmentation of projectiles and steel rings using numerical 3D simulations. In: 21th Int. Symp. Ballistics, 19–23 April, Adelaine, Australia; 2004.
[6] Rakvåg KG, Børvik T, Hopperstad OS. A numerical study on the deformation and fracture modes of steel projectiles during Taylor impact test. Int J Solids Struct 2014:808–21.
[7] Garrison Jr WM, Moody NR. Ductile fracture. J Phys Chem Solids 1987;48:1035–74.
[8] McClintock FA. A criterion for ductile fracture growth of holes. J Appl Mech 1968;35:363.
[9] Rice JR, Tracey DM. On the ductile enlargement of voids in triaxial stress fields. J Mech Phys Solids 1969;17:201–17.
[10] Bao Y, Wierzbicki T. A comparative study on various ductile crack formation criteria. J Eng Mater Tech 2004;126:314–24.
[11] Bao Y, Wierzbicki T. On fracture locus in the equivalent strain and stress triaxiality space. Int J Mech Sci 2004;46:81–98.
[12] Johnson GR, Hoegfeldt JM, Lindholm US, Nagy A. Response of various metals to large torsional strains over a large range of strain rates- Part 2. Less ductile metals. J Eng Mater Technol 1983;105(1):48–53.

[13] Wilkins ML, Streit RD, Reaugh JE. Cumulative−strain damage model of ductile fracture: simulation and prediction of engineering fracture tests. UCRL-53058, R3763. 1980.
[14] Bai Y, Wierzbicki T. A new model of metal plasticity and fracture with pressure and lode dependency. Int J Plast 2010;24:1071−96.
[15] Gruben G, Hopperstad OS, Børvik T. Evaluation of uncoupled ductile fracture criteria for the dual −phase steel docol 600D. Int J Mech Sci 2012:133−46.
[16] Johnson GR, Cook WH. Fracture characteristics of three metals subjected to various strains, strain rates, temperatures and pressures. Eng Fract Mech 1985;21(1):31−48.
[17] Bodner SR, Rubin MB. Modeling of hardening at very high strain rates. J Appl Phys 1994;76(5):2742−7.
[18] Rule WK, Jones SE. A revised form for the Johnson-cook strength model. Int J Impact Eng 1998;21(8):609−24.
[19] Lindfors AJ. 6.0 Mulitipurpose round fragmentation studies. In experiments in support of the Raufoss multipurpose ammunition technology study (RMATS) program for FY 99, Naval Air Warfare Center Weapons Division, China Lake, CA 93555-6001. 2000.
[20] Moxnes JF, Prytz AK, Frøyland Ø, Klokkehaug S, Skriudalen S, Friis E, et al. Experimental and numerical study of the fragmentation of expanding warhead casings by using different numerical codes and solution techniques. Defence Technol 2014;10(2):161−76. http://dx.doi.org/10.1016/j.dt.2014.05009.
[21] Vogler TJ, Thornhill TF, Reinhart WD, Chhabildas LC, Grady DE, Wilson LT, et al. Fragmentation of materials in expanding tube experiments. Int J Impact Eng 2003;29:735−46.
[22] Hopson MV, Scott CM, Patel R. Computational comparison of homogeneous and statistical description of AerMet100 steel subjected to high strain rate loading. Int J Impact Eng 2011;38:451−5.
[23] Wang R. Modeling material responses by arbitrary Lagrangian Eulerian formulation and adaptive mesh refinement method. J Comput Phys 2010;229:1573−99.
[24] Goto DM, Becker R, Orzechowski TJ, Springer HK, Sunwoo AJ, Syn CK. Investigation of the fracture and fragmentation of explosive driven rings and cylinders. Int J Impact Eng 2008;35:1547−56.
[25] Gold VM, Baker EL. A model for fracture of explosive driven metal shells. Eng Fract Mech 2008;75:275−89.
[26] Benz W. In: Buchler JR, editor. In numerical modelling of nonlinear stellar pulsation. problems and prospects. Dordrecht: Kluwer Academic; 1990.
[27] Børve S, Omang M, Trulsen J. Regularized smoothed particle hydrodynamics with improved multi-resolution handling. J Comput Phys 2005;208:345−67.
[28] Gray JP, Monaghan JJ, Swift RP. SPH elastic dynamics. Comput Meth Appl Mech Eng 2001;190:6641−62.
[29] Olovsson L, Hanssen AG, Børvik T, Langseth M. A particle-based approach to close-range blast loadings. Eur J Mech A Solids 2010;29(1):1−6.
[30] Børvik T, Olovsson L, Hanssen AG, Dharmasena KP, Hansson H, Wadley HNG. A discrete particle approach to simulate the combined effect of blast and sand impact loading of steel plates. J Mech Phys Solids 2011;59:940−58.
[31] Rohr I, Nahme H, Thoma K. Material characterization and constitutive modelling of ductile high strength steel for a wide range of strain rates. Int J Impact Eng 2005;31(4):401−33.
[32] Regazzoni G, Kocks UF, Follansbee PS. Dislocation kinetics at high strain rates. Acta Metall 1987;35(12):2865−75.
[33] Ferguson WG, Kumar A, Dorn JE. Dislocation damping in aluminum at high strain rates. J Appl Phys 1967;38:1863.
[34] Ott E. Shadowing theorem, chaos in dynamical systems. New York: Cambridge University Press; 1993. p. 18−9.